Organic X-Ray Image Sensors Using a Medium Bandgap Polymer Donor with Low Dark Current

Jong-Woon Ha (iD)*, Seung Hun Eom, Bo Kyung Cha, Seyeong Song, Hyeong Ju Eun, Jong H. Kim, Jong Mok Park, BongSoo Kim, Byoungwook Park, Seo-Jin Ko, Sung Cheol Yoon, Changjin Lee, In Hwan Jung* (iD)*, and Do-Hoon Hwang**

The development of portable X-ray detectors is necessary for diagnosing fractures in unconscious patients in emergency situations. However, this is quite challenging because of the heavy weight of the scintillator and silicon photodetectors. The weight and thickness of X-ray detectors can be reduced by replacing the silicon layer with an organic photodetectors. This study presents a novel bithienopyrroledione-based polymer donor that exhibits excellent photodetection properties even in a thick photoactive layer (~700 nm), owing to the symmetric backbone and highly soluble molecular structure of bithienopyrroledione. The ability of bithienopyrroledione-based polymer donor to strongly suppress the dark current density ($J_d \sim 10^{-10}$ A cm^{-2}) at a negative bias (-2.0 V) while maintaining high responsivity ($R = 0.29$ A W^{-1}) even at a thickness of 700 nm results in a maximum shot-noise-limited specific detectivity of $D_{sh}^* = 2.18 \times 10^{13}$ Jones in the organic photodetectors. Printed organic photodetectors are developed by slot-die coating for use in X-ray detectors, which exhibit $D_{sh}^* = 2.73 \times 10^{12}$ Jones with clear rising (0.26 s) and falling (0.29 s) response times upon X-ray irradiation. Detection reliability is also proven by linear response of the X-ray detector, and the X-ray detection limit is 3 mA.

1. Introduction

Organic photodetectors (OPDs), which can directly convert electromagnetic radiation into photocurrent signals, have attracted considerable attention owing to their use in optical communication, image sensing, biomedical sensing, machine vision, remote control, and X-ray detection.[1–7] In particular, the superior light absorption coefficient ($\varepsilon \approx 10^4$–10^5 cm^{-1}) of organic photoactive materials to silicon-based ones enables the fabrication of thin photoactive layers (<1 μm) *via* the solution process.[8,9] Such thin-film photodetecting layers can reduce the weight and simplify the fabrication process of OPDs, leading to portable and cheap light-detecting systems. Especially, portable X-ray detectors are necessary for diagnosing fractures in unconscious patients during emergencies. However, their development has been hampered by the heavy weight of the scintillator and silicon photodetectors. To reduce the weight and thickness of X-ray detectors,[10–13] a direct conversion X-ray detection strategy incorporating nanoparticles or scintillators into the bulk-heterojunction (BHJ) matrix is an effective strategy.[14–18] However, most BHJs in direct/indirect X-ray detectors are limited to poly(3-hexylthiophene) (P3HT) and [6,6]-Phenyl C$_{71}$ butyric acid methyl ester (PCBM), which suffer from the high dark current density (J_d) under applied reverse bias.[14,18,19] To address the aforementioned issue, the implementation of thick photoactive layers could effectively minimize J_d, but the short diffusion length of organic materials also limits photocurrent generation.[20] Moreover, thick photoactive layers can suppress pinhole formation and reduce defects, making them a promising approach for large-area process. Thus, the

Dr. J.-W. Ha, Prof. D.-H. Hwang
Department of Chemistry, Chemistry Institute for Functional Materials, Pusan National University, Busan 46241, Korea
E-mail: dohoonhwang@pusan.ac.kr
Dr. J.-W. Ha, Dr. S. H. Eom, Dr. B. Park, Dr. S.-J. Ko, Dr. S. C. Yoon, Dr. C. Lee
Division of Advanced Energy Materials Research Center, Korea Research Institute of Chemical Technology (KRICT), Daejeon 34114, Korea
Dr. B. K. Cha
Electro-Medical Device Research Center, Korea Electrotechnology Research Institute (KERI), Ansan 15588, Korea
Dr. S. Song
Graduate School of Carbon Neutrality, School of Energy and Chemical Engineering, Ulsan National Institute of Science and Technology (UNIST), Ulsan 44919, Korea
H. J. Eun, Prof. J. H. Kim
Department of Molecular Science and Technology, Ajou University, Suwon 16449, Korea

Dr. J. M. Park
Research Center for Advanced Specialty Chemicals, Korea Research Institute of Chemical Technology, Ulsan 44412, Korea
Prof. B. Kim
Department of Chemistry, Ulsan National Institute of Science and Technology (UNIST), Ulsan 44919, Korea
Prof. I. H. Jung
Department of Organic and Nano Engineering, Human-Tech Convergence Program, Hanyang University, 222 Wangsimni-ro, Seongdong-gu, Seoul 04763, Korea

development of thick OPDs with low J_d is one of the most important factors for commercialization.

For efficient photodetection in OPDs, the photoactive layer should exhibit a high responsivity (R) but a low J_d.[21] R denotes the photo-induced current density (J_{ph}) per unit irradiated light power (P_{in}). It can be improved by developing high-absorbance photoactive materials and creating a finely mixed bicontinuous nanomorphology between the electron donor and electron acceptor. In contrast, J_d is primarily determined by the charge carrier injection rate from each low/high work function electrode into the photoactive materials under dark conditions.[22–24] Thus, balanced hole/electron injection barriers can minimize J_d in OPDs. Cao and co-workers studied the dependence of OPD performance on inverted and conventional device architectures.[25] They found that similar electron/hole injection barriers (1.48 eV/1.50 eV) in the inverted structure resulted in a lower J_d than that in the conventional structure (0.88 eV/1.50 eV). More importantly, the formation of a thick film via the solution process is highly important for not only suppressing J_d in the devices but also applying the slot-die coating process to fabricate large-scale devices. A thick active layer reduces extrinsic defects, resulting in a lower probability of soft breakdown above a certain electric field and a higher effective barrier for charge injection. However, it simultaneously decreases charge transport and accelerates charge recombination in the active layer, thereby reducing the R value.[26–29] Thus, developing polymer donors featuring high hole mobility even with a thick photoactive layer is crucial for low J_d but high R values in the OPDs. However, only a few organic semiconductors have been reported to exhibit high R in a thick photoactive layer over 1 µm.[30,31] Our research group reported thieno[3,4-c]pyrrole-4,6-(5H)-dione (TPD)-based polymer donors that exhibited an excellent spectral R of $0.37\ A\ W^{-1}$ and a significantly suppressed J_d $(3.72 \times 10^{-9}\ A\ cm^{-2})$ even in a thick photoactive layer of 1 µm.[20] This resulted in a promising specific shot-noise-limited detectivity (D_{sh}^*) of 1.13×10^{13} Jones because of the high charge carrier mobility and the highly crystalline property of TPD-based polymers in the photoactive layer. Considering the high radiation dose of X-rays and the low scintillation efficiency (3–15%), the detection of low-intensity light is highly important in the OPDs for X-ray detectors.

In this study, a polymer with a medium band gap that can efficiently absorb the wavelength of light of 530 nm scintillated from X-ray irradiation and has a low J_d due to a deep-lying the highest occupied molecular orbital (HOMO) energy level of polymer donor. For this purpose, a new polymer donor (namely PBDT-biTPD) was designed and synthesized using bithienopyrroledione (biTPD) as an electron-accepting building block, BDT as a donor building block, and thienothiophene as a π-bridge. Devices based on PBDT-biTPD displayed highly promising OPD performance with a minimized J_d of $\sim 10^{-10}\ A\ cm^{-2}$ and a high R value of $0.29\ A\ W^{-1}$ under an applied reverse bias of -2.0 V, even for a ~ 700 nm thick photoactive layer, due to the high charge carrier mobility and bi-continuous interpenetrating network in the donor/acceptor blend film. In addition, the more numerous alkylation sites on the biTPD monomer could improve the solubility of the polymer in common organic solvents, making it possible to fabricate printed X-ray detectors via the slot-die coating process. Finally, we obtained clear X-ray photodetecting properties using the printed OPDs to demonstrate their potential in portable devices.

2. Results and Discussion

2.1. Synthesis and Characterization

PBDT-biTPD was synthesized via Stille cross-coupling polymerization of distannylated BDT and dibrominated biTPD monomers in the presence of a $Pd(PPh_3)_4$ catalyst. The systematic synthetic routes are shown in Schemes S1 and S2, Supporting Information.[32] The synthesized polymer donor exhibited excellent solubility in common chlorine-containing solvents such as chloroform, chlorobenzene, and o-dichlorobenzene, owing to the dual alkylation of the biTPD moiety. The molecular weight of PBDT-biTPD was measured by gel permeation chromatography (GPC) with o-dichlorobenzene as an eluent at 100 °C to avoid strong molecular interactions between the polymer molecules. The measured number average molecular weight (M_n) and dispersity ($Đ$) of PBDT-biTPD were 24 000 g mol^{-1} and 3.53, respectively. Thermogravimetric analysis (TGA) and differential scanning calorimetry (DSC) were performed to investigate the thermal behavior of the synthesized polymer. The measured thermal decomposition temperature (T_d, 5% weight loss) of PBDT-biTPD was 351.3 °C, and its glass transition temperature (T_g) was 168.74 °C, as shown in Figure S2, Supporting Information. PBDT-biTPD exhibits excellent thermal stability and low thermal segmental movement in the film state. The detailed molecular structures of the electron donor (PBDT-biTPD) and two acceptors ($PC_{70}BM$ and IT-4F) are shown in **Figure 1a**. The optical properties of PBDT-biTPD, $PC_{70}BM$, and IT-4F in the thin-film state measured using UV–Vis spectroscopy are shown in Figure 1b. The optical parameters are summarized in **Table 1**. The maximum absorption peak of PBDT-biTPD in the film state appeared at 639 nm, and its optical bandgap was calculated to be 1.80 eV from the absorption edge at 688 nm.

The electrochemical properties were estimated using cyclic voltammetry (CV), as shown in Figure S3, Supporting Information. The HOMO and the lowest unoccupied molecular orbital (LUMO) energy levels were estimated from the first oxidation and reduction onsets of CV, respectively. The HOMO energy level of PBDT-biTPD was quite deep (-5.36 eV) due to the strong electron-withdrawing strength of biTPD. Detailed schematic energy levels of PBDT-biTPD, $PC_{70}BM$, and IT-4F are shown in **Figure 2c**. The well-matched energy levels between the polymer donor (PBDT-biTPD) and electron acceptors ($PC_{70}BM$ and IT-4F) are suitable for efficient charge transport in the devices. Because of the low bandgap absorption of IT-4F, the PBDT-biTPD:IT-4F photoactive layer is beneficial for broadband OPDs covering the Vis-near infrared signal range. At the same time, owing to the low-lying HOMO energy level of $PC_{70}BM$, the PBDT-biTPD:PC_{70}-BM photoactive layer is more advantageous for blocking J_d in the OPDs.

2.2. Properties of OPDs

Bulk-heterojunction (BHJ) OPD devices with the structure of indium-tin-oxide (ITO)/ZnO/photoactive layer/MoO$_x$/Ag were fabricated to evaluate their photodetection performances. The thickness of the photoactive layer (from 200 to 1000 nm) was varied to find the optimal thickness that lead to low J_d but high J_{ph} in the OPDs. The results are shown in Figures S4 and S5 and Tables S1 and S2, Supporting Information. By increasing the thickness of PBDT-biTPD:PCBM from 200 to 1000 nm, J_d gradually decreased from 4.44×10^{-8} to
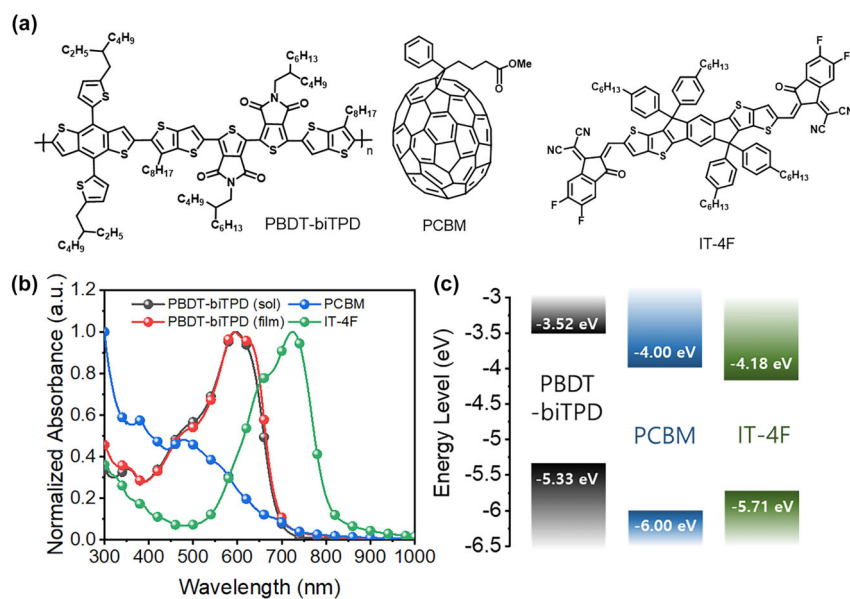
Figure 1. a) Molecular structure, b) optical properties, and c) energy-level diagram of the photoactive materials.

optimal R value of $0.29 \, \mathrm{A \, W^{-1}}$ with the lowest J_d value of $5.63 \times 10^{-10} \, \mathrm{A \, cm^{-2}}$. By contrast, as shown in Figure S5c, Supporting Information, the R value of the PBDT-biTPD:IT-4F device dropped significantly when the thickness exceeded 550 nm and reached $0.09 \, \mathrm{A \, W^{-1}}$ at ~1000 nm. The small changes of R in the PBDT-biTPD:PCBM device at different film thicknesses are more advantageous for increasing the R value as well as decreasing the J_d value, and this is attributed to excellent charge transport properties and fewer defect sites in the photoactive layer.[20]

The dependence of J_{ph} on the incident light intensity was measured at -2.0 V to investigate the characteristics of bimolecular charge recombination, as shown in Figure 2b. A linear slope closer to 1 means more effective suppression of bimolecular charge recombination.[34] The slope of the PBDT-biTPD:PCBM device ($\alpha = 0.99$) was significantly close to 1, but a slightly lower α value of 0.96 was observed in the PBDT-biTPD:IT-4F device. Therefore, the well-suppressed bimolecular charge recombination in the PBDT-biTPD:PCBM blended films could result in uniform R values over a large thickness range of the photoactive layer. In addition, charge carrier mobility is also important for increasing R value of the thick photoactive layer. Thus, the relationship between spectral R and charge carrier mobility was examined at different photoactive layer thicknesses using a photocharge carrier extraction method with a linearly increasing voltage.[35] The effective charge carrier mobilities were estimated using the equation $\mu = 2d^2/3At_{max}^2$ (if $\Delta j \ll j(0)$), where d is the photoactive layer thickness, A is the slope of a linearly increasing voltage pulse $(\mathrm{d}(V_t - V_0)/\mathrm{d}t)$, t_{max} is the time when the current reaches its highest value, $\Delta j = j(t_{max}) - j(0)$ is the current related to photoconductivity of the photoactive layer, and $j(0)$ is the capacitive step of the current. The results of photo-carrier extraction method with linearly increasing voltage (CELIV) are shown in Figure S6, Supporting Information. As determined from the photocurrent transients, the measured effective charge carrier mobilities of thin photoactive layers (ca. 200 nm) were 1.20×10^{-4} and $2.04 \times 10^{-4} \, \mathrm{cm^2 \, Vs^{-1}}$ for PBDT-biTPD:PCBM and PBDT-biTPD:IT-4F, respectively. These values for thin photoactive layers are similar, both on the scale of $10^{-4} \, \mathrm{cm^2 \, Vs^{-1}}$. In contrast, for a thick photoactive layer of ~700 nm, the charge carrier mobility of the PBDT-biTPD:PCBM blend film was still as high as $\sim 10^{-4} \, \mathrm{cm^2 \, Vs^{-1}}$, whereas that of the PBDT-biTPD:IT-4F blend film dropped significantly to

$5.03 \times 10^{-10} \, \mathrm{A \, cm^{-2}}$, and it became saturated at approximately $10^{-10} \, \mathrm{A \, cm^{-2}}$ when the thickness exceeded 700 nm. A similar trend was also observed in the PBDT-biTPD:IT-4F devices, which showed a low J_d value of $6.19 \times 10^{-10} \, \mathrm{A \, cm^{-2}}$ when using a thick photoactive layer of ~1000 nm. Increasing the thickness of the photoactive layer was highly efficient in decreasing the J_d values of OPDs. According to the rough estimation by Kasap,[33] an ideal J_d ranges from 0.1 to $10 \, \mathrm{nA \, cm^{-2}}$ while the commercial detectors (based a-Si) employed generally have a J_d of only $< 50 \, \mathrm{nA \, cm^{-2}}$. Therefore, the measured J_d of OPD is significantly competitive with commercialized a-Si-based OPDs. More importantly, the J_{ph} values of PBDT-biTPD:PCBM remained sufficiently high as the photoactive layer became thicker. Thus, we could effectively suppress J_d without significantly sacrificing J_{ph} in the devices, which is a highly desirable characteristic to increase both R and D* in the OPDs.

The spectral R was measured from the external quantum efficiency (EQE) using the equation (as depicted in Figures S4c and S5c, Supporting Information) $R = EQE \times \lambda/1240$. Here, λ is the wavelength of incident light in nanometers. As shown in Figure S4c, Supporting Information, the R value of PBDT-biTPD:PCBM device remained uniform when the thickness changed from 200 to 700 nm. Thus, at the thickness of 700 nm, the PBDT-biTPD:PCBM device showed the

Table 1. Optical and electrochemical properties of the photoactive materials.

	M_n [g mol^{-1}]	PDIs	λ_{edge} [nm] Film	E_g^{opt} [eV][a]	E_{HOMO} [eV][b]	E_{LUMO} [eV]
PBDT-biTPD	24 000	3.53	689	1.80	−5.36	−3.49
PCBM	—	—	726	1.71	−6.00	−4.00
IT-4F	—	—	801	1.55	−5.71	−4.18

[a] $E_g^{opt} = 1240/\lambda_{edge}$.
[b] $E_{HOMO \, or \, LUMO} = e(4.8 + E_{ox \, or \, red \, onset} - E_{ferrocene})$.
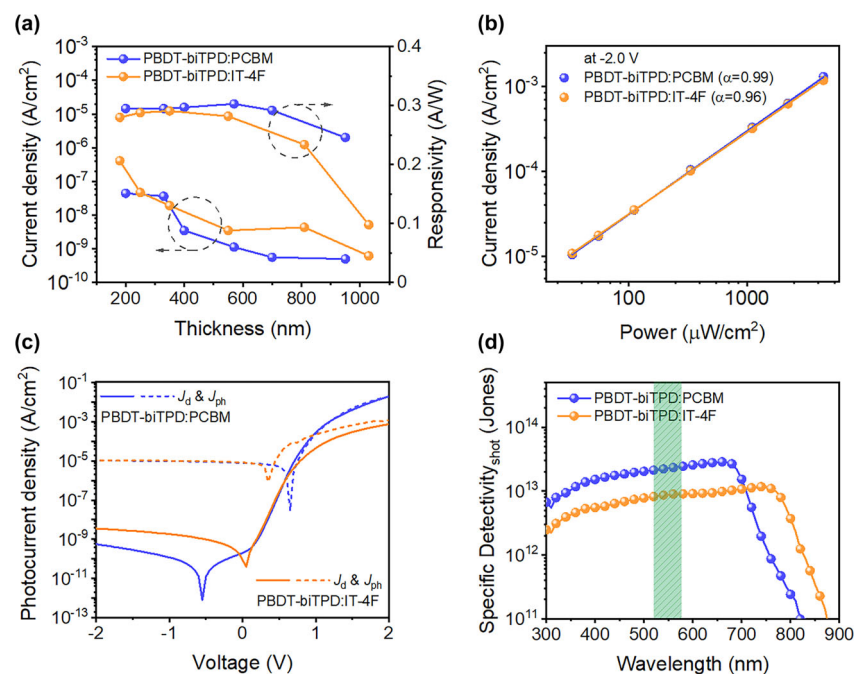
Energy & Environmental Materials

Figure 2. a) Dark current density and responsivity of OPDs depending on the photoactive layer thickness. b) Current density versus light intensity and c) J–V characteristics of the optimized OPDs in the dark and under 530-nm illumination. d) Shot-noise-limited specific detectivity of the optimum OPDs at −2.0 V.

$\sim 10^{-5}$ cm^2 Vs^{-1}. Consequently, the PBDT-biTPD:PCBM device, which featured a high charge carrier mobility for a thick photoactive layer (~ 700 nm), retained high R values under well-suppressed J_d conditions. In contrast, the significant EQE drops in thick PBDT-biTPD:IT-4F were closely associated with low carrier mobility. To investigate the linearity of the signal with regard to light intensity, the linear dynamic range (LDR) was measured using the equation LDR = $20\log(J_{ph}/J_d)$. The calculated LDR values of the PBDT-biTPD:PCBM and PBDT-biTPD:IT-4F devices were 85.3 and 69.7 dB, respectively. The PBDT-biTPD:PCBM device achieved a higher LDR value because of the well-suppressed J_d in the area under weak light irradiation.

The current–voltage (J–V) characteristics and spectral D_{sh}^* of the optimized OPDs are shown in Figure 2c,d, and the photodetecting properties are summarized in **Table 2**. The OPD properties of the PBDT-biTPD:PCBM (thickness: 700 nm) and PBDT-biTPD:IT-4F (thickness: 550 nm) devices were investigated under 530 nm green light irradiation at −2.0 V reverse bias. The shot-noise-limited detectivity (D_{sh}^*), which is a key figure-of-merit of photodetectors, was estimated from the measured R and J_d values of the J–V curves shown in Figure 2c, using the equation $D_{sh}^* = R/(2qJ_d)^{1/2}$, where q is the elementary charge. The PBDT-biTPD:PCBM device exhibited the best D_{sh}^* of 2.18×10^{13} Jones because it maintained a high R under the lowest J_d

conditions. In contrast, the PBDT-biTPD:IT-4F device showed a lower D_{sh}^* of 8.40×10^{12} Jones owing to the relatively high J_d level.

To better understand the relationship between the OPD performance and the photoactive layer thickness, we investigated the internal structures of the PBDT-biTPD:PCBM and PBDT-biTPD:IT-4F devices by cross-sectional transmission electron microscopy (TEM) observation. Because vertical phase segregation between electron donor and acceptor contributes to effectively suppressed J_d in the OPD.[36] Figure S7a–d, Supporting Information show the inverted device stack with a configuration of glass/ITO/ZnO/photoactive layer/MoO$_x$/Ag. Thin ($\sim$200 nm) and thick (570–710 nm) photoactive layers were fabricated to compare the effect of photoactive layer thickness on the internal structure. The distribution of S in the PBDT-biTPD:PCBM blend films was quantified using energy-dispersive X-ray spectroscopy (EDS) for both the cross-sectional and top-down specimens (Figure S7e,f, Supporting Information). Because only PBDT-biTPD contains S atoms, the bright green S regions indicate PBDT-biTPD-rich domains and the dark regions correspond to PCBM-rich domains. For the PBDT-biTPD:IT-4F blended films, EDS F mapping was performed to distinguish PBDT-biTPD and IT-4F (Figure S7g,h, Supporting Information) because only IT-4F contains F atoms. Thus, the bright blue F regions indicate the IT-4F-rich domains, and the dark regions correspond to the PBDT-biTPD-rich domains. The enlarged mapping EDS images of the cross-sectional specimens show that the polymer donor (PBDT-biTPD) and electron acceptor (PCBM or IT-4F) were uniformly mixed and distributed throughout the photoactive layer regardless of the photoactive layer thickness (see Figure S7i–l, Supporting Information). It was found that J_d of OPDs was dominated by just photoactive layer thickness regardless of the vertical phase segregation between electron donor and acceptor. From the perspective J_{ph},[20,37] the isotropic distribution of PBDT-biTPD and the electron acceptor (PCBM or IT-4F) allows efficient dissociation and extraction of charge carriers in the photoactive layer (Figure S7i–l, Supporting Information). This supports the ability of PBDT-biTPD-based devices to maintain high R values for a thick photoactive layer. The surface morphology of the blend films was investigated using atomic force microscopy (AFM) in the tapping mode, as shown in **Figure 3**a–d. The PBDT-biTPD:PCBM blends exhibit a well-defined and uniform morphology with a low root mean square (RMS) roughness of $\sim$1.7 nm. The PBDT-biTPD:IT-4F blend films exhibit clear nanofibrillar structures with slightly higher RMS values (>3.0 nm). Both blend films have a uniform and bicontinuous

Table 2. Detailed photodetecting performance of the OPDs at −2.0 V bias.

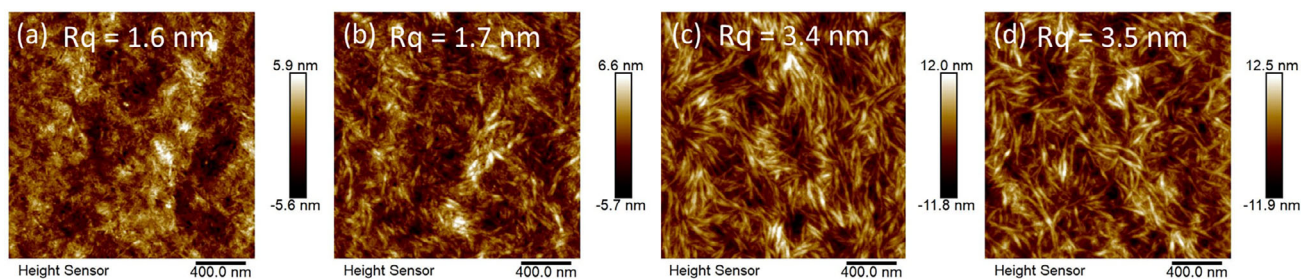|	Thickness [nm]	J_{ph} [A cm^{-2}]	J_d [A cm^{-2}]	R [A W^{-1}]	D_{sh}^* [Jones]	LDR [dB]
PBDT-biTPD:PCBM	700	1.04×10^{-5}	5.63×10^{-10}	0.29	2.18×10^{13}	85.3
PBDT-biTPD:IT-4F	550	1.08×10^{-5}	3.52×10^{-9}	0.28	8.40×10^{12}	69.7

Figure 3. AFM images of PBDT-biTPD:PCBM at a) 220 and b) 710 nm and PBDT-biTPD:IT-4F at c) 200 and d) 570 nm photoactive layer thicknesses.

nano-network between the donor and acceptor, which is favorable for exciton dissociation and charge carrier transport in the OPDs.

2.3. Organic X-Ray Detectors

It is widely known that direct measurement of the noise current based on J_d generally underestimates the noise of an OPD, leading to D^* overestimation.[35] Therefore, we investigated the total noise current, including the shot, thermal, and flicker noises, based on the specific detectivity (D_n^*) of PBDT-biTPD:PCBM using the equation $D_n^* = RA^{1/2}/S_n$, where A and S_n denote the device area and noise spectral density, respectively. In general, the noise power density of OPDs tends to be strongly dependent in the low-frequency region ($\sim 1/f$ relationship) and becomes saturated in the high-frequency region.[38] Interestingly, however, the PBDT-biTPD:PCBM device exhibited frequency-independent noise in the whole frequency region under a reverse bias of -2.0 V, as shown in **Figure** 4a. This indicates that mostly white noise exists in the PBDT-biTPD:PCBM blend films with negligible flicker noise. The specific D_n^* was measured by the extracted noise current in the range of 1–40 Hz, and the corresponding D_n^* of the PBDT-biTPD:PCBM device was 3.91×10^{12} Jones at 530 nm. Subsequently, the response times of PBDT-biTPD:PCBM were measured under green light irradiation. The cutoff frequency at -3 dB ($f_{-3\text{ dB}}$) was examined using frequency-modulated input light signals. This is the frequency at which the output electrical signal reaches 0.707 times the initial electrical signal while retaining the amplitude of the input light

signal.[39] As shown in Figure 4c, the measured $f_{-3\text{ dB}}$ value of PBDT-biTPD:PCBM was 17.8 kHz.

Printed PBDT-biTPD:PCBM devices were developed using slot-die coating for use in portable X-ray image sensors. **Figure** 5a shows the characteristic J–V curves of the printed OPDs based on PBDT-biTPD:PCBM blend films. The printed PBDT-biTPD:PCBM devices exhibited a spectral R of 0.26 A W^{-1} under -2.0 V reverse bias, and the estimated D_{sh}^* was 2.73×10^{12} Jones under 530-nm light irradiation. Despite the slot-die coating process, the OPD performance stayed sufficiently high, which is a great advantage of PBDT-biTPD:PCBM devices for retaining a constant R value at different photoactive layer thicknesses. **Figure** 6a shows a schematic of the demonstration setup for X-ray image sensors. The X-ray tube employed in this experiment was originally used to image the human body (Figure S8, Supporting Information). The X-ray detection system, scintillator, and OPD assembly were placed on a stage. The operating conditions of the X-ray source were: a tube voltage of 70 kV, a tube current of 10–80 mA, and an exposure time of 2 s. The distance between the X-ray source and the scintillator-coupled organic device was 100 cm. The X-ray image sensor consisting of the scintillator and printed PBDT-biTPD:PCBM OPD were exposed to X-ray pulses with an on-time of 2 s and an off-time of 12 s, as shown in Figure 6b. The X-ray detector confirmed that the on/off process was continuous over time, and similar response times were obtained for different beam currents. The measured rising response times (from 10% to 90%) and falling response times (from 90% to 10%) of the OPDs were 0.26 and 0.29 s, respectively. The rising/falling response time of typical X-ray OPDs is measured in microseconds, but in our case, it is somewhat slower. This is believed to be because the thick photoactive
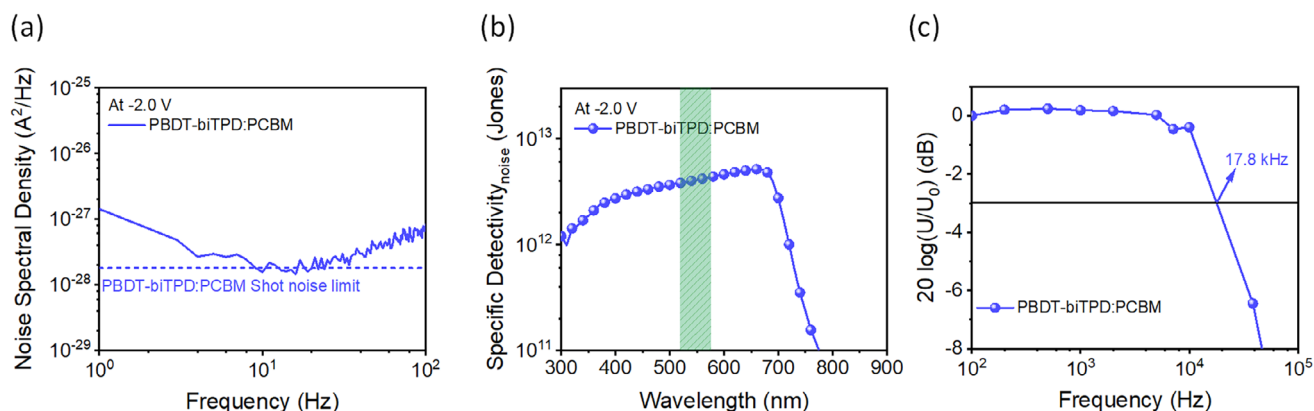

Figure 4. a) Noise spectral density and b) specific detectivity based on measured total noise for the OPD comprising PBDT-biTPD:PCBM. c) Normalized response as a function of frequency of the optimum OPD under 530-nm illumination at -2.0 V.
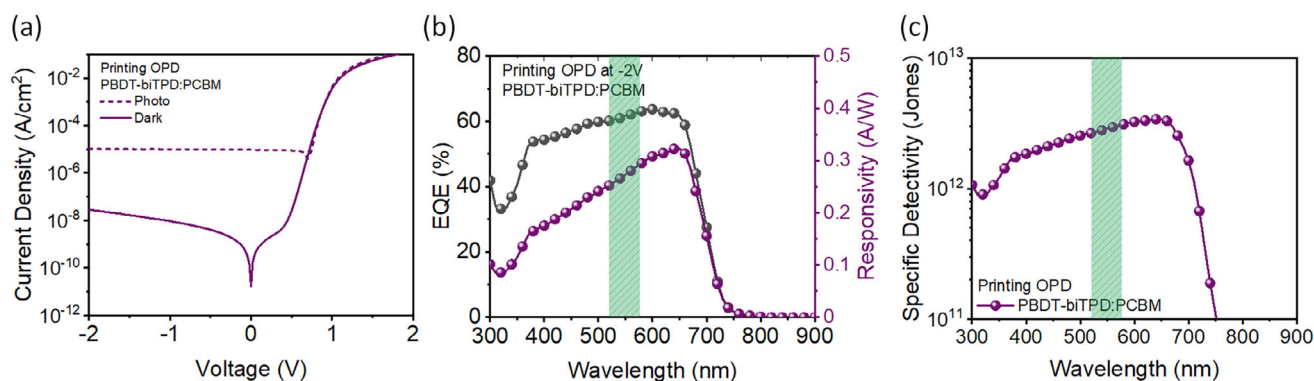
Figure 5. a) *J–V* characteristics of printed OPD comprising PBDT-biTPD:PCBM in the dark and under 530-nm illumination. b) EQE and responsivity curves and c) shot-noise-limited specific detectivity of printed OPD at −2.0 V.
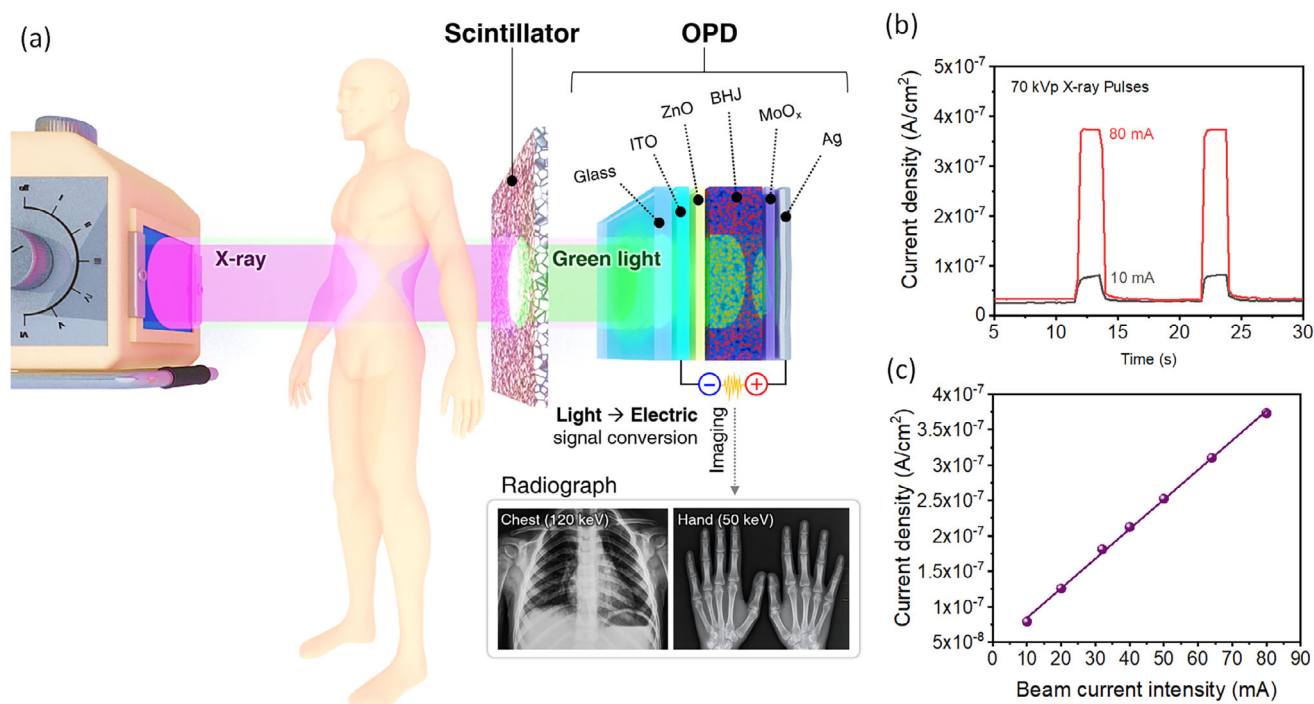

Figure 6. a) Schematic of the demonstration setup for X-ray detection application. b) Response characteristics of the X-ray detector and c) current density of the printed OPD versus beam current intensity of the X-ray.

layer of PBDT-biTPD:PCBM reduces the capacitance and thus affects the RC constant.[40,41] We noticed that the detector exhibited a steady and continuous current density at both X-ray intensities (i.e., beam current intensity, shown in Figure S9, Supporting Information), which was mainly attributed to the well-suppressed J_d of PBDT-biTPD:PCBM. Finally, Figure 6c shows that the current generated (or induced) in the OPD gradually increased according to the intensity of the scintillated light during X-ray irradiation. The detection limit of the PBDT-biTPD:PCBM device was calculated from the intersection point of the slope shown in Figure 6c, and the J_d value (2.81×10^{-18} A cm^{-2}) to be as low as 3.23 mA. Owing to the low J_d and excellent linearity of J_{ph} according to the X-ray beam intensity, the PBDT-biTPD:PCBM OPD enables X-ray imaging even with weak exposure. In this study, the highest current density generated in the printed OPD occurred at the X-ray tube voltage of 70 kV and current of 80 mA. The reliability of the X-ray detector was also proven by the linearity upon adjusting the amount of scintillation light *via* increasing the tube current from 10 to 80 mA.

3. Conclusions

Owing to the high radiation dose of X-rays and low scintillation efficiency (3–15%), the ideal OPDs in X-ray detectors should be able to

detect low light intensities, which requires decreasing J_d while retaining high J_{ph} values. To satisfy these requirements, a green light-sensitive polymer donor, PBDT-biTPD, was designed and synthesized. The biTPD-based polymer (PBDT-biTPD) is highly advantageous for increasing charge transport even when using a thick photoactive layer (550–700 nm). In addition, dialkylation of the biTPD monomer improved the solubility of PBDT-biTPD as well as its miscibility with various electron acceptors (PCBM and IT-4F), resulting in a highly uniform and bicontinuous nanomorphology in a thick photoactive layer of 550–700 nm. Due to the well-suppressed J_d ($\sim 10^{-10}\,\mathrm{A\,cm^{-2}}$) at a negative bias ($-2.0$ V) while maintaining a high R value (0.29 A W^{-1}) even at a layer thickness of 700 nm, the PBDT-biTPD:PCBM devices showed a highly promising D_{sh}^* of 2.18×10^{13} Jones at -2.0 V. In addition, PBDT-biTPD:PCBM displayed only white noise current at all frequencies, inducing a high total-noise-based specific detectivity of 3.91×10^{12} Jones. Moreover, printed OPDs were successfully fabricated by slot-die coating, and they showed clear rise (0.26 s) and fall (0.29 s) response times upon X-ray irradiation. Notably, reliable X-ray detection was also proven by the linear response upon adjusting the tube current from 10 to 80 mA to tune the amount of scintillation light, and the X-ray detection limit was 3 mA. The practicality of using an X-ray detector in a medical setup was also successfully demonstrated.

4. Experimental Section

Poly(3-(5-(4,8-bis(5-(2-ethylhexyl)thiophen-2-yl)benzo[1,2-*b*:4,5-*b'*]dithiophen-2-yl)-6-octylthieno[3,2-*b*]thiophen-2-yl)-5,5'-bis(2-butyloctyl)-3'-(6-octylthieno[3,2-*b*]thiophen-2-yl)-4*H*,4'*H*-[1,1'-bithieno[3,4-*c*]pyrrole]-4,4',6,6'(5*H*,5'*H*)-tetraone) (PBDT-biTPD) was synthesized using a previously reported method.[S1] All other reagents were purchased from Sigma-Aldrich and used as received without further purification. Thermal analyses (TGA and DSC) were performed using Q600 (TA Instruments) under an inert N$_2$ atmosphere, with heating/-cooling rates of 10 °C min^{-1}. Ultraviolet-visible spectra were recorded using a UV-visible spectrophotometer (UV-1800). To determine the molecular weight and confirm the polydispersity index (PDI) of the polymers, gel permeation chromatography (GPC) was performed using *o*-dichlorobenzene solution (Polymers Lab) at a flow rate of 1.0 mL min^{-1} and 100 °C with polystyrene standards. Cyclic voltammetry experiments were performed using an electrochemical analyzer (CH Instruments) in acetonitrile solutions containing 0.1 M tetrabutylammonium tetrafluoroborate (Bu$_4$NBF$_4$) as the supporting electrolyte, with Ag/AgNO$_3$ as the reference electrode, a platinum wire as the counter electrode, and a platinum working electrode. The thickness of the active layer was measured using a KLA Tencor Alpha-step IQ surface profilometer with an accuracy of ± 1 nm. The *J–V* characteristics of OPDs were measured under green LED light (THORLABS, M530L3) in the range of 0.33–5.56 mW cm^{-2}. The light intensity was calibrated using a standard photodiode power sensor (THORLABS, S120C) with a compact power and energy meter console. Electronic data were recorded using a Keithley 236 source measure unit, and all characterizations were performed in an ambient environment. The external quantum efficiency (EQE) was measured as a function of wavelength between 300 and 900 nm using a halogen lamp as the light source, and calibration was performed using a silicon reference photodiode. The measurements were performed after masking all but the active cell area of the fabricated device. All characterization steps were performed under ambient laboratory conditions.

4.1. General Polymerization Procedure

A mixture of the distannylated monomer (1 equiv.), the dibrominated monomer (1 equiv.), and tetrakis(triphenylphosphine)palladium(0) (0.03 equiv.) was prepared in anhydrous toluene (5 mL) and *N*,*N*-dimethylformamide (DMF, 1 mL).

This reaction mixture was stirred at 110 °C for 16 h, and subsequently added with 2-tributylstannylthiophene (0.2 mL) and 2-bromothiophene (0.2 mL). After 2 h, the reaction mixture was poured into methanol (200 mL), and the precipitate was collected by filtration and purified via Soxhlet extraction using methanol, acetone, and hexane. The copolymers were obtained by re-precipitation of the chloroform solution in methanol. This method was used to synthesize PBDT-biTPD from biTPD (300.0 mg, 0.23 mmol), BDT (208.8 mg, 0.23 mmol), and Pd(PPh$_3$)$_4$ (8.0 mg). GPC results: $M_n = 24\,000$ g mol^{-1}, PDI = 3.53. $T_d = 351.3$ °C.

4.2. Device Fabrication by Spin-coating

Bulk-heterojunction OPDs were fabricated with an inverted structure consisting of indium tin oxide (ITO)/ZnO/photoactive layer/MoO$_3$/Ag. Typically, a $\sim$30 nm ZnO layer as an electron-transporting layer was coated onto ITO after pre-cleaning the latter with UV-ozone plasma. The active layer material was dissolved in chlorobenzene (total concentration: 30–60 mg mL^{-1}) and spin-coated at various coating speeds for 30 s in a glove box filled with argon. After drying the active layer, MoO$_x$ ($\sim$8 nm) and Ag ($\sim$100 nm) layers were formed *via* thermal evaporation under a base pressure of 10^{-7} Torr. The effective area of the device was 9 mm^2.

4.3. Device Fabrication by Printing

Bulk-heterojunction OPDs were fabricated with an inverted structure consisting of ITO/ZnO/photoactive layer/MoO$_3$/Ag. Typically, a $\sim$30 nm ZnO layer as an electron-transporting layer was coated onto ITO after pre-cleaning the latter with UV-ozone plasma. Slot-die coater with a width of 7 mm slot-die head was used for fabricating electron-transporting and photoactive layers. The photoactive materials were dissolved in chlorobenzene (total concentration: 40 mg mL^{-1}) and used for slot-die coating with a flow rate of 50 uL s^{-1} and a coating speed of 10–20 mm s^{-1} at room temperature in a glove box filled with argon. After drying the active layer, MoO$_x$ ($\sim$8 nm) and Ag ($\sim$100 nm) layers were formed *via* thermal evaporation under a base pressure of 10^{-7} Torr. The effective area of the device was 9 mm^2.

Conflict of Interest

The authors declare no conflict of interest.

Supporting Information

Supporting Information is available from the Wiley Online Library or from the author.

[1] K.-J. Baeg, M. Binda, D. Natali, M. Caironi, Y.-Y. Noh, *Adv. Mater.* **2013**, *25*, 4267.

[2] D. Baierl, L. Pancheri, M. Schmidt, D. Stoppa, G.-F. Dalla Betta, G. Scarpa, P. Lugli, *Nat. Commun.* **2012**, *3*, 1175.

[3] R. D. Jansen-van Vuuren, A. Armin, A. K. Pandey, P. L. Burn, P. Meredith, *Adv. Mater.* **2016**, *28*, 4766.

[4] G. Konstantatos, E. H. Sargent, *Nat. Nanotechnol.* **2010**, *5*, 391.

[5] D. Li, X. Liu, G. Dong, L. Duan, D. Zhang, H. Zhao, L. Wang, Y. Qiu, *Laser Photonics Rev.* **2014**, *8*, 316.

[6] W. Pan, H. Wu, J. Luo, Z. Deng, C. Ge, C. Chen, X. Jiang, W.-J. Yin, G. Niu, L. Zhu, L. Yin, Y. Zhou, Q. Xie, X. Ke, M. Sui, J. Tang, *Nat. Photonics* **2017**, *11*, 726.

[7] X. Wang, Z. Cheng, K. Xu, H. K. Tsang, J.-B. Xu, *Nat. Photonics* **2013**, *7*, 888.

[8] N. Strobel, N. Droseros, W. Köntges, M. Seiberlich, M. Pietsch, S. Schlisske, F. Lindheimer, R. R. Schröder, U. Lemmer, M. Pfannmöller, N. Banerji, G. Hernandez-Sosa, *Adv. Mater.* **2020**, *32*, 1908258.

[9] S. Yoon, J. Ha, J. Cho, D. S. Chung, *Adv. Opt. Mater.* **2016**, *4*, 1933.

[10] B. Yang, L. Yin, G. Niu, J.-H. Yuan, K.-H. Xue, Z. Tan, X.-S. Miao, M. Niu, X. Du, H. Song, E. Lifshitz, J. Tang, *Adv. Mater.* **2019**, *31*, 1904711.

[11] X. Zhao, G. Niu, J. Zhu, B. Yang, J.-H. Yuan, S. Li, W. Gao, Q. Hu, L. Yin, K.-H. Xue, E. Lifshitz, X. Miao, J. Tang, *J. Phys. Chem.* **2020**, *11*, 1873.

[12] S. O. Kasap, J. A. Rowlands, *J. Mater. Sci. Mater. Electron.* **2000**, *11*, 179.

[13] F. Arca, S. F. Tedde, M. Sramek, J. Rauh, P. Lugli, O. Hayden, *Sci. Rep.* **2013**, *3*, 1324.

[14] H. M. Thirimanne, K. D. G. I. Jayawardena, A. J. Parnell, R. M. I. Bandara, A. Karalasingam, S. Pani, J. E. Huerdler, D. G. Lidzey, S. F. Tedde, A. Nisbet, C. A. Mills, S. R. P. Silva, *Nat. Commun.* **2018**, *9*, 2926.

[15] A. Ciavatti, L. Basiricò, I. Fratelli, S. Lai, P. Cosseddu, A. Bonfiglio, J. E. Anthony, B. Fraboni, *Adv. Funct. Mater.* **2019**, *29*, 1806119.

[16] A. Intaniwet, C. A. Mills, M. Shkunov, P. J. Sellin, J. L. Keddie, *Nanotechnology* **2012**, *23*, 235502.

[17] M. P. A. Nanayakkara, L. Matjačić, S. Wood, F. Richheimer, F. A. Castro, S. Jenatsch, S. Züfle, R. Kilbride, A. J. Parnell, M. G. Masteghin, H. M. Thirimanne, A. Nisbet, K. D. G. I. Jayawardena, S. R. P. Silva, *Adv. Funct. Mater.* **2021**, *31*, 2008482.

[18] P. Büchele, M. Richter, S. F. Tedde, G. J. Matt, G. N. Ankah, R. Fischer, M. Biele, W. Metzger, S. Lilliu, O. Bikondoa, J. E. Macdonald, C. J. Brabec, T. Kraus, U. Lemmer, O. Schmidt, *Nat. Photonics* **2015**, *9*, 843.

[19] D. J. Starkenburg, P. M. Johns, J. E. Baciak, J. C. Nino, J. Xue, *J. Appl. Phys.* **2017**, *122*, 225502.

[20] J. B. Park, J.-W. Ha, S. C. Yoon, C. Lee, I. H. Jung, D.-H. Hwang, *ACS Appl. Mater. Interfaces* **2018**, *10*, 38294.

[21] G. Simone, M. J. Dyson, S. C. J. Meskers, R. A. J. Janssen, G. H. Gelinck, *Adv. Funct. Mater.* **2020**, *30*, 1904205.

[22] X. Zhou, D. Yang, D. Ma, *Adv. Opt. Mater.* **2015**, *3*, 1570.

[23] H. Shekhar, O. Solomeshch, D. Liraz, N. Tessler, *Appl. Phys. Lett.* **2017**, *111*, 223301.

[24] A. Pierre, I. Deckman, P. B. Lechêne, A. C. Arias, *Adv. Mater.* **2015**, *27*, 6411.

[25] G. Liu, T. Li, X. Zhan, H. Wu, Y. Cao, *ACS Appl. Mater. Interfaces* **2020**, *12*, 17769.

[26] J. Wu, J. Luke, H. K. H. Lee, P. Shakya Tuladhar, H. Cha, S.-Y. Jang, W. C. Tsoi, M. Heeney, H. Kang, K. Lee, T. Kirchartz, J.-S. Kim, J. R. Durrant, *Nat. Commun.* **2019**, *10*, 5159.

[27] Z. Shang, T. Heumueller, R. Prasanna, G. F. Burkhard, B. D. Naab, Z. Bao, M. D. McGehee, A. Salleo, *Adv. Energy Mater.* **2016**, *6*, 1601149.

[28] G. Zhang, R. Xia, Z. Chen, J. Xiao, X. Zhao, S. Liu, H.-L. Yip, Y. Cao, *Adv. Energy Mater.* **2018**, *8*, 1801609.

[29] L. Ma, S. Zhang, H. Yao, Y. Xu, J. Wang, Y. Zu, J. Hou, *ACS Appl. Mater. Interfaces* **2020**, *12*, 18777.

[30] D. Zhang, B. Fan, L. Ying, N. Li, C. J. Brabec, F. Huang, Y. Cao, *SusMat* **2021**, *1*, 4.

[31] T. L. Nguyen, H. Choi, S. J. Ko, M. A. Uddin, B. Walker, S. Yum, J. E. Jeong, M. H. Yun, T. J. Shin, S. Hwang, J. Y. Kim, H. Y. Woo, *Energ. Environ. Sci.* **2014**, *7*, 3040.

[32] J.-W. Ha, H. J. Park, I.-N. Kang, D.-H. Hwang, *Dyes Pigm.* **2022**, *200*, 110176.

[33] S. O. Kasap, *J. Phys. D* **2000**, *33*, 2853.

[34] I. Fraga Domínguez, A. Distler, L. Lüer, *Adv. Energy Mater.* **2017**, *7*, 1601320.

[35] G. Juška, K. Arlauskas, M. Viliūnas, J. Kočka, *Phys. Rev. Lett.* **2000**, *84*, 4946.

[36] T. Agostinelli, M. Campoy-Quiles, J. C. Blakesley, R. Speller, D. D. C. Bradley, J. Nelson, *Appl. Phys. Lett.* **2008**, *93*, 203305.

[37] W. Wang, X. Miao, G. Cai, L. Ding, Y. Li, T. Li, Y. Zhu, L. Tao, Y. Jia, Y. Liang, X. Lu, Y. Fang, Y. Yi, Y. Lin, *Adv. Mater.* **2022**, *34*, 2201600.

[38] J.-W. Ha, H. J. Eun, B. Park, H. Ahn, D. R. Hwang, Y. S. Shim, J. Heo, C. Lee, S. C. Yoon, J. H. Kim, S.-J. Ko, *Adv. Funct. Mater.* **2023**, *33*, 2211486.

[39] M. Biele, C. Montenegro Benavides, J. Hürdler, S. F. Tedde, C. J. Brabec, O. Schmidt, *Adv. Mater. Tech.* **2019**, *4*, 1800158.

[40] K. An, C. Kim, K. H. Cho, S. Bae, B. K. Cha, K.-T. Kang, *Org. Electron.* **2022**, *100*, 106384.

[41] J. Liu, J. Jiang, S. Wang, T. Li, X. Jing, Y. Liu, Y. Wang, H. Wen, M. Yao, X. Zhan, L. Shen, *Small* **2021**, *17*, 2101316.